atmosphere

MDPI

Article

Water Tank Experiments on Stratified Flow over Double Mountain-Shaped Obstacles at High-Reynolds Number

Ivana Stiperski [1,*], Stefano Serafin [2], Alexandre Paci [3], Hálfdán Ágústsson [4], Anne Belleudy [3], Radiance Calmer [3], Kristian Horvath [5], Christoph Knigge [6], Johannes Sachsperger [2,7], Lukas Strauss [2] and Vanda Grubišić [8]

1 Institute of Atmospheric and Cryospheric Sciences, University of Innsbruck, 6020 Innsbruck, Austria
2 University of Vienna, Department of Meteorology and Geophysics, 1090 Vienna, Austria; stefano.serafin@univie.ac.at (S.S.); johannes.sachsperger@univie.ac.at (J.S.); lukas.strauss@univie.ac.at (L.S.)
3 CNRM, UMR 3589, Météo-France/CNRS, 31100 Toulouse, France; alexandre.paci@meteo.fr (A.P.); anne.belleudy@meteo.fr (A.B.); radiance.calmer@meteo.fr (R.C.)
4 Kjeller Vindteknikk, 2027 Kjeller, Norway; halfdan.agustsson@vindteknikk.no
5 Meteorological and Hydrological Service, Zagreb 10000, Croatia; kristian.horvath@cirus.dhz.hr
6 Institute of Meteorology and Climatology, Leibniz Universität Hannover, 30419 Hannover, Germany; knigge@muk.uni-hannover.de
7 MeteoServe GmbH, 1220 Vienna, Austria
8 National Center for Atmospheric Research, Boulder, CO 80301, USA; vanda.grubisic@ucar.edu
* Correspondence: ivana.stiperski@uibk.ac.at; Tel.: +43-512-507-54454

Academic Editor: Robert Talbot
Received: 7 November 2016; Accepted: 10 January 2017; Published: 13 January 2017

Abstract: In this article, we present an overview of the HyIV-CNRS-SecORo (Hydralab IV-CNRS-Secondary Orography and Rotors Experiments) laboratory experiments carried out in the CNRM (Centre National de Recherches Météorologiques) large stratified water flume. The experiments were designed to systematically study the influence of double obstacles on stably stratified flow. The experimental set-up consists of a two-layer flow in the water tank, with a lower neutral and an upper stable layer separated by a sharp density discontinuity. This type of layering over terrain is known to be conducive to a variety of possible responses in the atmosphere, from hydraulic jumps to lee waves and highly turbulent rotors. In each experiment, obstacles were towed through the tank at a constant speed. The towing speed and the size of the tank allowed high Reynolds-number flow similar to the atmosphere. Here, we present the experimental design, together with an overview of laboratory experiments conducted and their results. We develop a regime diagram for flow over single and double obstacles and examine the parameter space where the secondary obstacle has the largest influence on the flow. Trapped lee waves, rotors, hydraulic jumps, lee-wave interference and flushing of the valley atmosphere are successfully reproduced in the stratified water tank. Obstacle height and ridge separation distance are shown to control lee-wave interference. Results, however, differ partially from previous findings on the flow over double ridges reported in the literature due to the presence of nonlinearities and possible differences in the boundary layer structure. The secondary obstacle also influences the transition between different flow regimes and makes trapped lee waves possible for higher Froude numbers than expected for an isolated obstacle.

Keywords: laboratory experiments; lee-wave interference; mountain waves; rotors; stratified flows; valley flushing

1. Introduction

Topography covering the Earth's surface is mostly complex. Isolated ridges or mountains, although a useful idealization for process understanding, are rarely found in reality, though notable exceptions exist, e.g., [1–4]. Nevertheless, most of the literature on stable flow over mountains still focuses on mountain waves forming over isolated obstacles, e.g., [5–12].

As a step towards more realistic topography, one can examine the flow of stably stratified fluid over double obstacles, where linear and non-linear interactions of waves forming over each obstacle can be expected. Earliest studies of flow over double obstacles [13–15] suggest that a systematic variation of wave amplitude can occur when waves generated by the first obstacle are in or out of phase with those generated by the second obstacle. This phenomenon was termed as lee-wave interference. Subsequent laboratory experiments and numerical simulations of flows over double obstacles separated by a valley, performed in the 1980s, e.g., [16–18], mainly focused on flow conditions within the valley and identified important dimensionless parameters governing the flow: Froude number (Fr), ridge separation distance (V) and horizontal wavelength of the terrain-generated waves (λ). Tampieri and Hunt [16] recognized that when the lee-wave wavelength is similar to or larger than the ridge separation distance, the valley atmosphere can be flushed (or ventilated) out of the valley by terrain-following shooting flow.

The question of lee-wave interference and its influence on wave drag received renewed attention only recently. Laboratory experiments [19], analytical [20] and numerical modeling [21,22] confirmed that the secondary obstacle changes the character of the flow and can systematically alter the wave amplitude downstream and affect the wave drag. Indications of the existence of lee-wave interference have also been gathered during the Terrain-Induced Rotor Experiment (T-REX) [23], and its predecessor, the Sierra Rotors Project that took place in the Owens Valley, California. Real-case numerical simulations and aircraft observations during T-REX [24–27] showed a rapid decay of wave amplitude downstream of the Inyo Mountains, suggestive of destructive lee-wave interference.

Grubišić and Stiperski [28] and Stiperski and Grubišić [29] used idealized two-dimensional numerical simulations to systematically study lee-wave interference of waves trapped by wind shear and its effect on rotors. Rotors, turbulent horizontal vortices found in the lee of topography, form when the boundary layer separates from the surface due to the adverse pressure gradient force caused by topographically induced gravity waves, e.g., [27,30–33]. Stiperski and Grubišić [29] showed that the variations of lee-wave amplitude due to interference depend linearly on the ratio between ridge separation distance and wavelength of the lee waves in the lee of a single obstacle both for free-slip and no-slip simulations. However, destructive interference was identified to be a non-linear process, as was the response of lee-wave rotors to changes in the lee-wave amplitude. When the ridge separation distance favored destructive interference, maximum destructive interference downstream of double obstacles was found to occur when the secondary obstacle was approximately two-thirds of the height of the primary one. This was shown to be a consequence of surface friction, causing attenuation of wave amplitude downstream of the obstacles [9,10]. Secondary terrain, even substantially smaller than primary, was found to significantly modify the flow response in a realistic setting [34].

Inspired by the results of Stiperski and Grubišić [29] and laboratory experiments of Knigge et al. [32] that successfully reproduced rotor flow in a stratified water tank, HyIV-CNRS-SecORo (Hydralab IV–CNRS–Secondary Orography and Rotors Experiments) water tank experiments, made possible through the Hydralab IV initiative, were designed to study the effect of secondary orography on stratified flow and rotors. For this purpose, a large number of experiments were performed with different obstacle heights and ridge separation distances. Laboratory experiments were performed to complement numerical simulations, since turbulence in laboratory experiments is directly generated and not parameterized as in numerical models. Therefore, these experiments can be used to verify simulation results, in particular the models' dynamical core and turbulence parametrizations. Additionally, unlike large field campaigns, laboratory experiments offer controlled repeatable conditions that allow systematic study of the phenomenon in question. To be applicable for

atmospheric flows, however, laboratory experiments are required to have both density stratification and high Reynolds number. These conditions are rarely met simultaneously in the same facility, but the CNRM (Centre National de Recherches Météorologiques) large stratified water flume in Toulouse was designed especially for this purpose.

HyIV-CNRS-SecORo laboratory experiments were initialized with a density profile chosen in analogy to [32,35] with a neutral layer close to the surface, separated from a stably stratified layer above by a density jump. This profile is often encountered upstream of the mountains, and is different from the one used in the numerical study of Stiperski and Grubišić [29] where vertical wind shear was used to trap the waves. Given that waves trapped on the inversion (i.e., density jump) are surface waves and therefore different in nature to those trapped by positive shear (cf. [36,37]), the overall goals of HyIV-CNRS-SecORo experiments were to:

1. Test the applicability of wave interference theory to waves trapped on the inversion in dependence on the ratio of ridge separation distance (V) to horizontal lee-wave wavelength (λ);
2. Examine the influence of the secondary obstacle height and reproduce conditions under which waves in the lee of the obstacle are totally cancelled;
3. Examine the influence of lee-wave interference on rotors;
4. Reproduce hydraulic jump rotors and examine the influence of secondary obstacles on them;
5. Examine the inner structure of rotor turbulence.

The purpose of this paper is to present the concept of the laboratory measurements and highlight the first results. In particular, we focus on the first and second question concerning the existence of lee-wave interference and the influence of the height of the secondary obstacle. In Section 2, we discuss in detail the experimental design and data processing. Section 3 describes the results for single and double obstacles. The results and implications are discussed in Section 4 and conclusions drawn in Section 5.

2. Methods

2.1. Experimental Design

The experiments were carried out in the large stratified water flume at the geophysical fluid dynamics laboratory of CNRM in Toulouse (France). This facility was used in recent years for studies of boundary layers and internal waves [38], in particular those topographically induced and trapped at a density jump, e.g., [39,40]. The flume was used here as a 22-m-long, 1-m-high, 3-m-wide closed glass tank (Figure 1). A glass wall divided the tank into two parts, respectively 0.5 m and 2.5 m wide. The obstacles were towed in the narrow part of the tank, while the wide part was used to dampen waves propagating horizontally from the two ends of the smaller part. Those waves were reflected into the wider part of the tank by deflectors covered with wave-damping material (Figure 1a,c). The openings at the two ends of the smaller part also acted to minimize the upstream perturbation caused by flow blocking for Froude number lower than 1. This design is different from the one used in Knigge et al. [32] and is optimized towards running a large number of experiments, as was required to address the objectives of this study. In particular, the larger part of the tank acted as a "reservoir" of density stratification so the tank did not need to be refilled in order to rebuild the density interface as often as in the configuration used by [32].

The stratification was controlled using salinity, while the laboratory air and water temperature was regulated at 20 °C. Water in the tank was supplied by two pumps connected to two reservoirs filled respectively with freshwater and brine. The flow of each pump was controlled by a computer, in order to achieve the desired density profile. The mixture of freshwater and brine was then diffused through floating diffusers on the free surface. The surface diffuser procedure was used in order to get a density jump as sharp as possible (an example of measured profile is given on Figure 2). The density profile was measured before and after each experiment in the fluid at rest using a carefully calibrated conductivity probe. The upper layer had a constant Brunt-Väisälä frequency N, defined as

$$N = \sqrt{-\frac{g}{\rho_0}\frac{\partial \rho}{\partial z}} \quad (1)$$

N ranged between 0.5 and 0.87 s^{-1} for the different experiments.

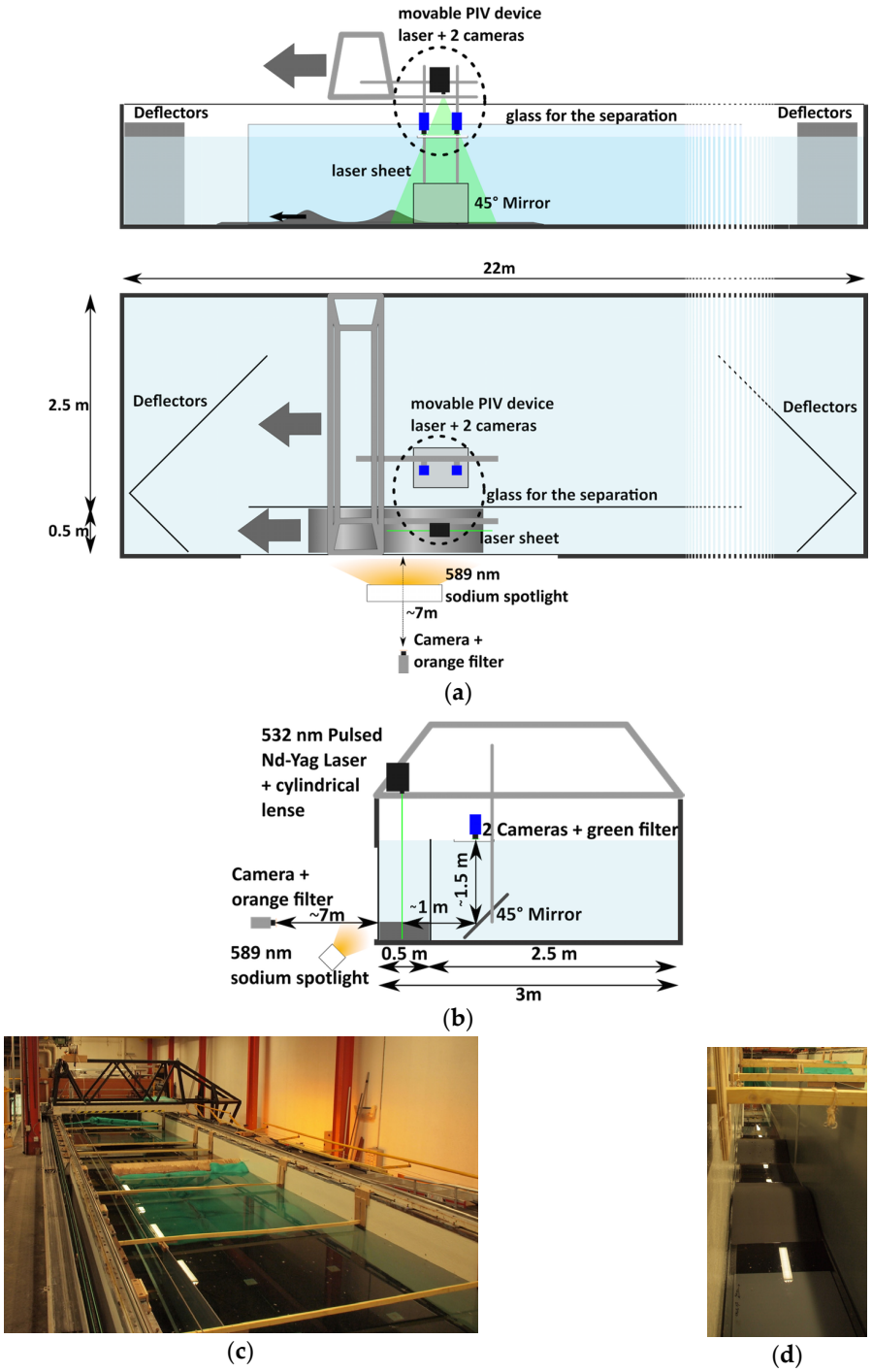

Figure 1. From top to bottom: (**a**) cross-section along the longer side of the water tank and the view from the top; (**b**) the cross-section along the shorter side of the CNRM large stratified water flume set-up used for the experiments; (**c**) photograph of the water tank; (**d**) photograph of the narrow part of the tank with the obstacles.

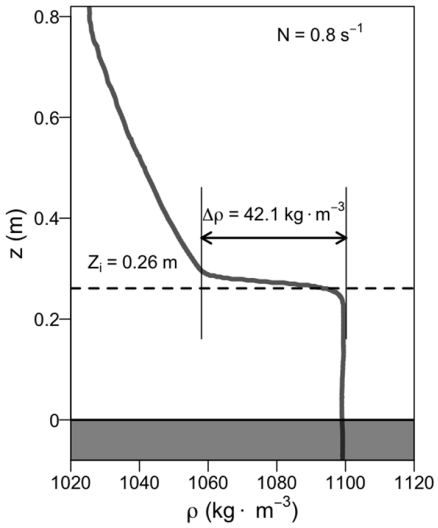

Figure 2. Example of a density profile for experiment 242. The depth of the mounting plate for the obstacles is indicated with a shaded area at the bottom of the plot.

The obstacle (one or two mountains separated by a given distance) was mounted on a long plate attached to a moving bank (Figure 1a,d), and moving in the same direction using a double pulley system at a prescribed constant speed U. The plate extended significantly upstream (50 cm) and downstream of the obstacle in order to reproduce a no-slip boundary condition in both parts. The obstacles and the plate were made of PVC (PlyVinyl Chloride) and colored with paint to increase their roughness (similar to [32]), which was on the order of several tenths of millimeters. Twenty-four additional single obstacle experiments were conducted with a 1 m long plate mounted upstream of the obstacle and covered by lego elements in order to increase the roughness and explore the influence of surface friction on the flow.

The obstacle shapes were Gaussian, defined by

$$\begin{array}{ll} h_i(x) = H_i \exp(-\frac{x^2}{2L^2}), & 0 \le |x| \le L_{0i} \\ h_i = 2.1mm, & |x| = L_{0i} \\ h_i = 0\,mm, & |x| > L_{0i} + 2\,cm \end{array} \quad (2)$$

with a smooth transition between $x = L_{0i}$ and $x = L_{0i}$ + 2 cm. Here, subscript i denotes the obstacle (first or second), L is the characteristic length scale of the obstacle shape and L_{0i} is the actual width of each obstacle. In total, four different obstacles were used in laboratory experiments, as indicated in Table 1. Unlike the quasi two-dimensional obstacles in Knigge et al. [32], the obstacles used in these experiments are fully two-dimensional (2D) and fill the lateral extent of the part of the tank in which they were pulled (Figure 1d). Still, the tallest obstacle is the same height and length as in Knigge et al. [32], and it was used for all the single obstacle experiments and as the upstream obstacle in all the double obstacle experiments. The other obstacles were used in experiments examining the influence of secondary obstacle height, and they correspond to three-thirds, two-thirds and one-third of the primary obstacle height.

Table 1. Physical dimensions of obstacles used in HyIV-CNRS-SecORo.

	H_i (m)	$2L^2$ (cm^2)	L_{0i} (cm)
Primary or Single (H_1)	13.2	1060	66.3
Secondary (H_2)	13.2	1060	66.3
Secondary (H_2)	8.8	1060	62.9
Secondary (H_2)	4.4	1060	56.8

During each experiment, two different optical measurements were used to measure the flow, seeded with light-reflecting particles. The first optical system used a fixed camera looking at the flow from an observational window about 10 m from the starting position (see Figure 1a,b). The flow was lit up over its entire width by two 120 W high-pressure sodium lamps. Images were taken using a two-megapixel Sensicam camera from the brand PCO, equipped with an 80-mm lens and a high pass filter with cut-off at 550 nm. The distance between the camera and the window was about 7 m, so the field of view was approximately 1.5 m. The second optical system used two cameras moving along with the obstacle (see Figure 1a). The flow was lit by a laser sheet from a two-headed pulsed Nd-Yag laser (532 nm) equipped with a cylindrical lens. Images were taken using two four-megapixel PCO 2000 cameras, equipped with 35 mm lenses and a low pass filter cutting at 550 nm. Cameras looked down at the flow from the top through a floating glass window and an underwater 45° mirror (see Figure 1b). The distance between the camera and the laser sheet was about 2.5 m, so the total field of view (combining both cameras) was about 1.2 m. A fixed video camera was also used to record the flow.

The Froude number for each experiment was calculated from the undisturbed density profile (Figure 2) and towing speed as (cf. [32,35]):

$$F_r = \frac{U}{\sqrt{g\frac{\Delta\rho}{\rho_0}Z_i}} \tag{3}$$

Here, U is the towing speed, ρ_0 is the density of the lower neutrally stratified layer capped by a density jump $\Delta\rho$, Z_i is the mean height of the density jump (i.e., inversion), and g is the acceleration due to gravity. The density increases linearly above the density jump. Use of scaled variable (e.g., Froude number F_r, non-dimensional inversion height H_1/Z_i) allows for transferability of the results of water tank measurements to the atmosphere [32].

In total, 395 experiments were conducted with single or double obstacles (H_2/H_1 ranging from 0 to 1, cf. Table 1) for a range of Froude numbers F_r extending from 0.17 to 1.4, and first obstacle height to inversion height ratio H_1/Z_i from 0.29 to 1.31. The non-linearity parameter NH_1/U in the upper stably stratified layer ranged between 0.3 and 2, with a median value of 0.65. For most of the experiments (85%) the flow in upper layer was linear ($NH_1/U < 1$) and non-hydrostatic since NL/U was below 0.1 for all experiments.

Since several experiments using the same set of H_2/H_1, H_1/Z_i and F_r were conducted; not all of the 395 experiments are unique. The full list of all the experiments is given in Table S1 (Supplementary Materials).

2.2. Data Processing

Data obtained from the experiments consist of high-resolution images taken with one fixed and two movable cameras. The high-resolution movable cameras were used to zoom in on the specific features of the wave field, in particular for the purpose of obtaining high-resolution velocities from Particle Image Velocimetry (PIV) in order to study inner turbulence structure of a rotor. These analyses are, however, outside the scope of this paper.

The aim of the fixed camera was to provide information on the entire flow field. Since it is impossible to cover the entire flow with the fixed camera's field of view, the regions downstream of both obstacles could not be captured in the same shot. Therefore, for the purpose of analyzing the inversion displacement in the lee of both obstacles, the original photographic data have been processed to create composite images (cf. Figure 3a). Narrow tiles at the center of the photographic frame were cut from different images and arranged side by side. The width of each tile corresponded to the distance travelled by the towing rack between two consecutive images. Therefore, given the constant shooting frequency, the width was adjusted to the towing speed. Composites are not instantaneous snapshots of the flow. They are, however, a good approximation of instantaneous frames if the flow remains stationary (with respect to the obstacle) between the first and the last picture of the

series. This condition is met for most the experiments discussed herein. The images used to produce composites can also be processed to compute velocities using PIV.

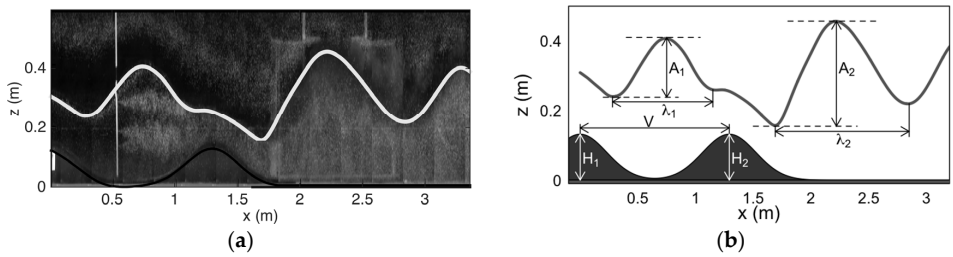

Figure 3. (**a**) Example of interface detection for experiment 240; (**b**) Schematic diagram showing the definition of variables used in the text.

The composites were used to obtain the height of the interface (inversion) displacement (Figure 3a) and from this to calculate the lee-wave amplitudes and wavelengths (Figure 3b). The interface detection was done manually due to difficulties in isolating the interface from other elements in the background and the turbulent blur occurring for some of the experiments. An example of manual interface detection is given in Figure 3a. The interface was detected by selecting pixels that correspond to the boundary between the two fluid layers. This coincided with the largest brightness gradient between the lower fluid layer having a larger concentration of light-reflecting particles (light colored area) and the darker upper layer with no or very few particles. This boundary itself was usually populated with a higher concentration of particles than either the layer below or above, which greatly facilitated interface detection. For cases of flow with large mixing (e.g., hydraulic jump), only the upper part of the boundary with the largest concentration of particles was chosen as the interface height, and therefore the manual detection was unable to isolate the small scale internal folding that might occur within the jump (cf. Figure 4c).

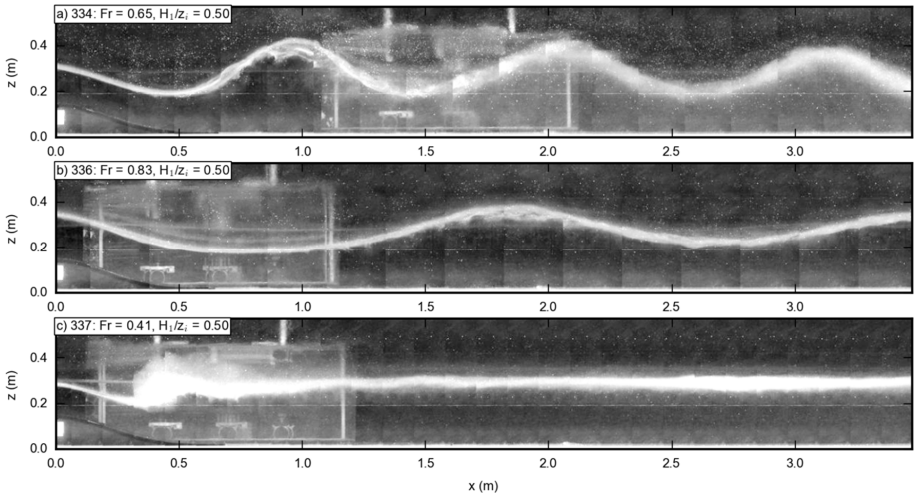

Figure 4. Examples of prototype flow regimes: (**a**) trapped lee wave; (**b**) long waves; (**c**) hydraulic jump.

Amplitudes within the valley (A_1) and downstream of the second peak (A_2) were calculated as the difference between minimum and maximum interface displacement within the relevant horizontal region (Figure 3b). The wavelength (λ_1 and λ_2) was determined as a physical distance between the consecutive minima (or maxima) of the first wave downstream of each obstacle. This definition was sometimes ambiguous, since the wavelength in some experiments evolved further downstream. From these variables, dimensionless ratios, governing lee-wave interference, were calculated following Stiperski and Grubišić [29]. These are:

- Amplitude ratios A_2/A_1 or A_2/A_s, where the numbers denote the obstacle downstream of which the amplitude was calculated (1, 2 and *s* for first, second and single, respectively).
- Mountain height ratio H_n, defined as the ratio of second to first obstacle height H_2/H_1.
- Dimensionless inversion height H_1/Z_i, defined as the ratio between first obstacle height and the inversion height.
- Dimensionless wavelength (V/λ), defined as ratio between valley width V, taken as the distance between the ridges of the obstacles, and the lee-wave wavelength.

2.3. Flow Classification

Experiments were classified based on the flow morphology into the following three regimes: trapped lee waves, long waves and hydraulic jumps. Examples of the regimes are given in Figure 4. The flow was classified as trapped lee waves when regular undulations formed in the lee of the obstacles, without noticeable mixing and the wavelength of the wave was smaller than the maximum wavelength for which waves can be trapped on the inversion (cf. [37])

$$\lambda \leq \lambda_{\max} = \frac{2\pi U}{N} \tag{4}$$

When the lee-wave wavelength (λ) exceeded this threshold, the flow was classified as long waves. Long waves (with $\lambda > \lambda_{max}$ are able to propagate vertically through the inversion and are then reflected at the free surface of the water tank. Since their trapping is not directly linked to the inversion, their characteristics are not governed by Froude number and dimensionless inversion height but by the stratification of the upper water layer and the water depth. These long waves were classified as trapped lee waves in [32], where they were also shown to be able to produce lee wave rotors.

For experiments to be classified as a hydraulic jump, a sudden jump in the interface and large accompanying mixing were required.

The most pronounced (largest amplitude) feature was used for classifying the entire experiment (e.g., large-amplitude trapped lee waves get precedence over long waves), despite the fact that the flow regime might be different in between the obstacles and downstream of them (see Section 3.2).

3. Results

In this section, we present results of the HyIV-CNRS-SecORo water tank experiments. We first focus on the experiments with an isolated obstacle and compare them to literature results obtained from other laboratory studies and numerical simulations. Afterwards, we examine the results from experiments with double obstacles and focus on the different aspects of the influence of the secondary obstacle on the flow.

3.1. Flow over an Isolated Obstacle

Even if the primary focus of HyIV-CNRS-SecORo was the influence of a secondary obstacle on the stably stratified flow, a significant part of the experiments (47%) were performed for flow over an isolated obstacle with different Froude numbers and dimensionless inversion heights. In addition to being a test of our experimental set-up, single obstacle experiments are used as a reference for experiments with double obstacles examined in Section 3.2 and are crucial for the scaling of wavelengths and amplitudes.

The wide range of governing parameters covered by the experiments allowed the reproduction of all prototypical flow regimes of interest, such as trapped lee waves (Figure 4a) and hydraulic jumps (Figure 4c) as also observed by Knigge et al. [32]. Additionally, long waves were observed in the water tank (Figure 4b). The transition between these different flow regimes occurs mainly through the variation of Froude number for a given dimensionless inversion height (Figure 5), and coincides with the increase of lee-wave wavelength with increasing Froude number; the same as observed by Vosper [35].

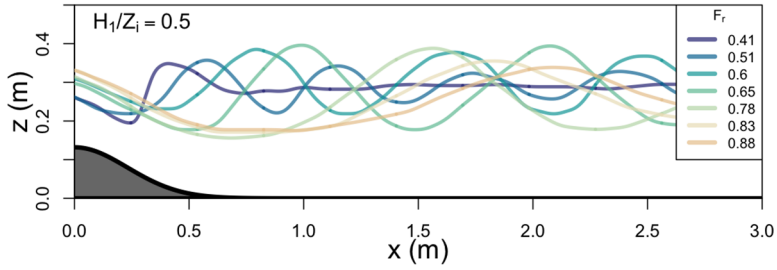

Figure 5. Interface displacement for a set of single obstacle runs with fixed H_1/Z_i = 0.5 and Fr ranging from 0.41 to 0.88, corresponding to flow regimes of hydraulic jump (F_r = 0.41), trapped lee waves (F_r = 0.51–0.78) and long waves (F_r = 0.83–0.88).

The differences in obstacle shape between HyIV-CNRS-SecORo and [32] (quasi 2D in [32] and fully 2D in our case), as well as flow conditions between the water tank experiments and Vosper's numerical simulations [35] as noted in [32], warrant a detailed comparison between our experiments and the previous ones. For that purpose, we summarize the flow classification in a regime diagram (Figure 6a) and compare it to [32,35]. The larger number of single obstacle experiments performed during HyIV-CNRS-SecORo than in [32] allows a better comparison of our experiments to Vosper's [35] regime diagram. The regime diagram for a single obstacle (Figure 6a) corresponds well to those obtained by both [32] and [35]. The limiting line between trapped lee waves and vertical propagating-wave regimes from [35] correctly delineates trapped lee waves from the long waves observed in the water tank. The small differences observed could be due to the fact that the Brunt–Väisälä frequency and therefore NH_1/U in the upper layer was not perfectly constant for all the experiments and therefore does not correspond exactly to the one used in [35]. This might allow some trapped waves to exist beyond the limiting line. The separation between trapped lee waves and hydraulic jumps fits qualitatively well to that from regime diagrams of both Knigge et al. [32] and Vosper [35], but is best described by the limiting line of Sachperger et al. [41]. We can therefore conclude that the differences in obstacle shapes and flow characteristics do not have important repercussions for our results, providing confidence in analyzing experimental results for double obstacles.

3.2. Flow over Double Obstacles

Regime diagrams for double obstacles (Figure 6b–d) are qualitatively similar to that for a single obstacle. Trapped lee waves, hydraulic jumps and long waves are observed in the relevant regime space. Still, a notable exception is obvious: trapped lee wave regime covers a larger portion of the regime space than for a single obstacle. Firstly, trapped lee waves occur even below the limiting line of Sachsperger et al. [41] where hydraulic jumps are expected. Secondly, trapped lee waves over double obstacles persist at higher Froude numbers than downstream of a single obstacle, despite the fact that NH_1/U (and therefore also the limiting line separating the two) is similar. In addition, flushing of the valley atmosphere (cf. [16]) is observed and is associated with waves whose wavelength is similar to or larger than the ridge separation distance and these are shown in Figure 6 with cross symbols.

The existence of trapped lee waves (that satisfy the criterion given by Equation (3)) at high Froude number is a surprising result since the same combination of governing parameters (F_r and H_1/Z_i) corresponds to long waves for a single obstacle and waves that propagate through the interface in the atmosphere according to [35]. The presence of a secondary obstacle thus forces a decrease of lee-wave wavelength that corresponds to a flow regime transition. An example of such a regime transition for H_1/Z_i = 0.9, Fr = 1.1 is given in Figure 7. Downstream of a single obstacle, this combination of Froude number and dimensionless inversion height results in long waves caused by wave reflection off the free water surface and is not governed by the trapping on the inversion. On the other hand, this same profile over double obstacles, leads either to valley flushing in between the obstacles and long waves downstream of them over a narrow valley or to large-amplitude trapped lee waves both in between

the obstacles and downstream of them over a wide valley. It is important to note that valley flushing (cf. [16]) is not exclusive to long waves that do not undergo regime transition, but occurs also for trapped lee waves.

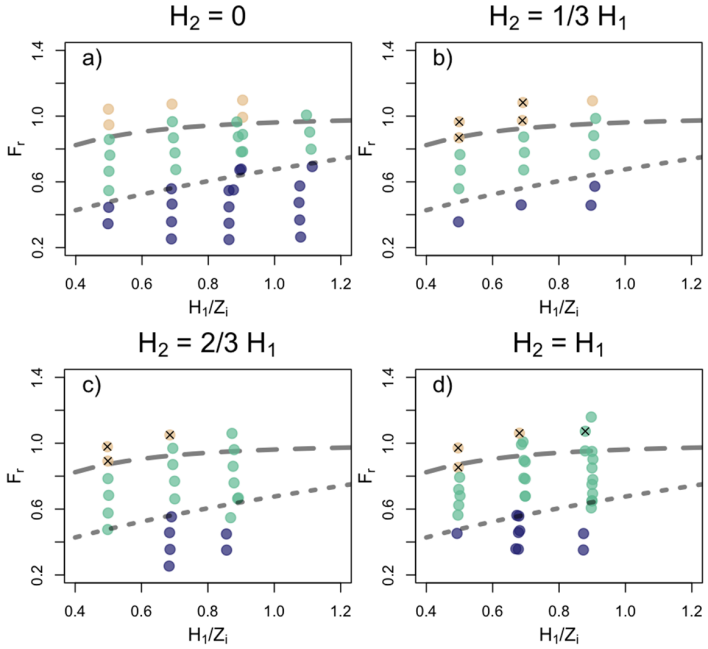

Figure 6. Regime diagram of HyIV-CNRS-SecORo experiments showing the dependence of flow type on Froude number *Fr* and dimensionless inversion height (H_1/Z_i) for the: (**a**) single obstacle runs; (**b**) runs where the secondary obstacle is one-third of the height of the first one; (**c**) the secondary obstacle is two-thirds of the height of the first one; and (**d**) for obstacles of equal height. The long-dashed line separates trapped lee waves from vertically propagating waves according to Vosper [35]. The short-dashed line separates hydraulic jumps from trapped lee waves according to Sachsperger et al. [41] with NH_1/U equal to 0.5. Crosses correspond to cases of valley flushing.

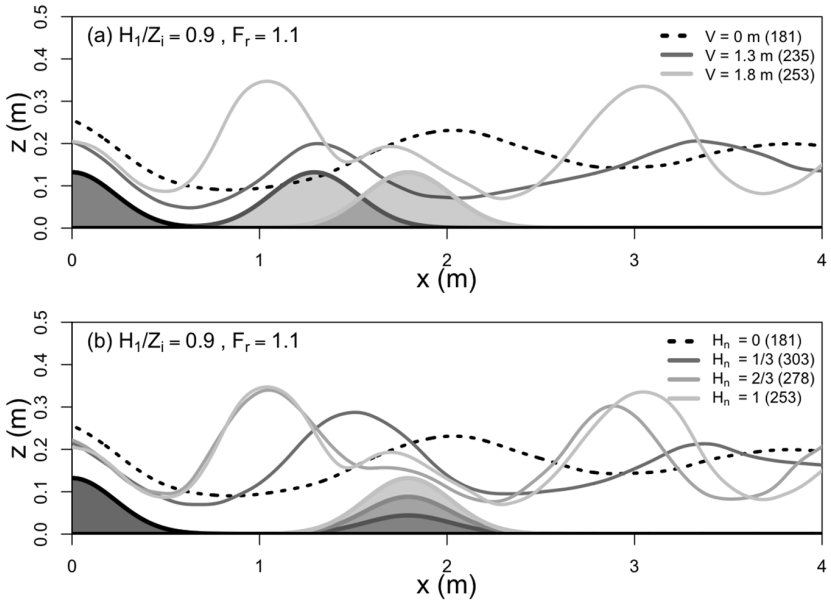

Figure 7. Interface displacement for a set of double obstacle runs with fixed H_1/Z_i = 0.9 and median F_r equal to 1.095, for (**a**) different valley widths; (**b**) different heights of the second obstacle.

The distinction between these two types of response (regime transition or valley flushing) is governed by the dimensionless wavelength (V/λ_s), but the regime transition is also strongly modulated by the second obstacle height. For the case where flow transitions to trapped lee waves, these large-amplitude trapped waves persist in between the obstacles for all mountain height ratios examined. Downstream of the second obstacle, however, the transition to trapped lee waves depends on mountain height ratio. When the second obstacle is low (e.g., H_n = 1:3), the regime transition does not occur downstream of it and flow there again has the form of long waves. It is possible that this regime transition occurs due to a decrease of lee-wave wavelength over the valley, caused by the presence of the second obstacle. These new shorter waves over the valley are no longer able to propagate through the inversion and are therefore trapped there causing their amplitude to increase. Stiperski and Grubišić [29] have observed the modulation of lee-wave wavelength by double obstacles caused by the fact that the Fourier transform of double obstacles has distinct maxima. A detailed study of this phenomenon is, however, beyond the scope of this paper but will be addressed in a future publication.

This is the first time, to our knowledge, that such a regime transition has been documented. Double obstacle regime diagrams (Figure 6b–d) indicate that this transition is not a rare occurrence but develops systematically. They show that, in the case of double obstacles, trapped lee waves can occur for much higher Froude number than over single obstacles and suggest a new dividing line between trapped lee waves and vertically propagating waves is warranted for water tank experiments, different from the one proposed by Vosper [35] for a single obstacle.

Both of these phenomena (regime transition and valley flushing) are therefore a complex interaction between non-linearity introduced by combination of F_r and H_1/Z_i [41] and complex topography through the relation between lee-wave wavelength and ridge separation distance. This non-linearity in flow response and differences in the flow character are also clear from the difference in interface height between single obstacle and double obstacle experiments in Figure 7. Flow over single obstacle is blocked upstream so that the interface rises high over the obstacle, whereas for double obstacle experiments flow is not blocked but undergoes supercritical transition leading to a lower interface height.

The existence of a secondary obstacle is expected to have a profound influence on trapped lee waves through the development of lee-wave interference as shown by Grubišić and Stiperski [28] and Stiperski and Grubišić [29]. This is despite the fact that these numerical studies use a considerably different upstream profile (constant stability profile and constant vertical wind shear) to trap the waves. The trapped lee wave water tank experiments indeed suggest that both constructive and destructive lee-wave interference (Figure 8) develops and show that the small variations in the location of the secondary obstacle significantly alter both the lee-wave amplitude and wavelength. Wavelength is generally reduced compared to single obstacle experiments, as also observed by Gyüre and Jánosi [19] albeit for a different upstream profile. The exact amount of wavelength reduction, however, is modulated by lee-wave interference. Obstacle separation is confirmed to be one of but not the only controlling parameter of both wavelength and amplitude change. An example in Figure 8 shows that a narrower valley (Figure 8a) causes a shortening of the wavelength and amplitude attenuation downstream of the secondary obstacle as compared to the wider valley (Figure 8b) where significant enhancement of wave amplitude occurs. The opposite is true for the example in Figure 9a where it is the wider valley that leads to wave attenuation. The difference between these two examples stems from the differences in lee-wave wavelength (a function of F_r and H_1/Z_i, different for the two experiments) that causes the waves downstream of the first obstacle to be in or out of phase with those generated by the second obstacle, over the same ridge separation distance. The second obstacle height also considerably modifies lee-wave amplitude and wavelength (Figure 9b). In this example, the effect of the second obstacle is maximized for larger H_2 as the higher second obstacle causes a larger reduction of wave amplitude. This, however, is not always the case as will be discussed later in this section.

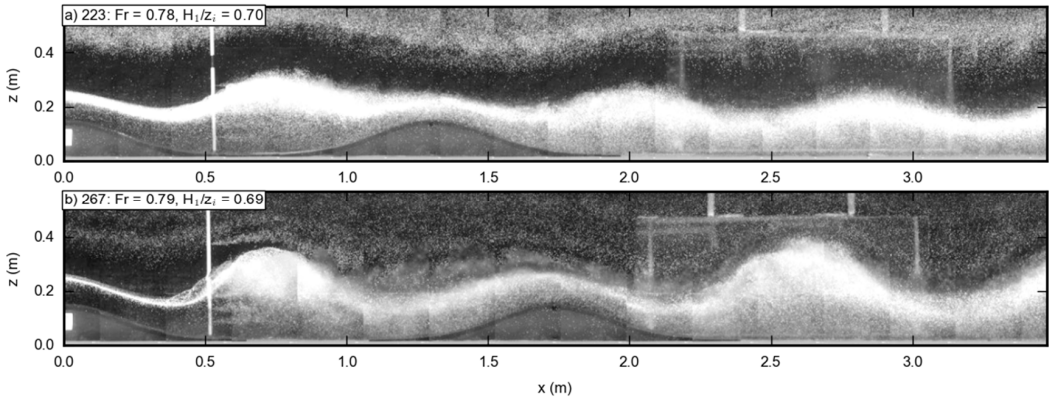

Figure 8. Examples of (**a**) destructive and (**b**) constructive lee-wave interference for (**a**) shorter 1.3 m and (**b**) longer 1.8 m valley width.

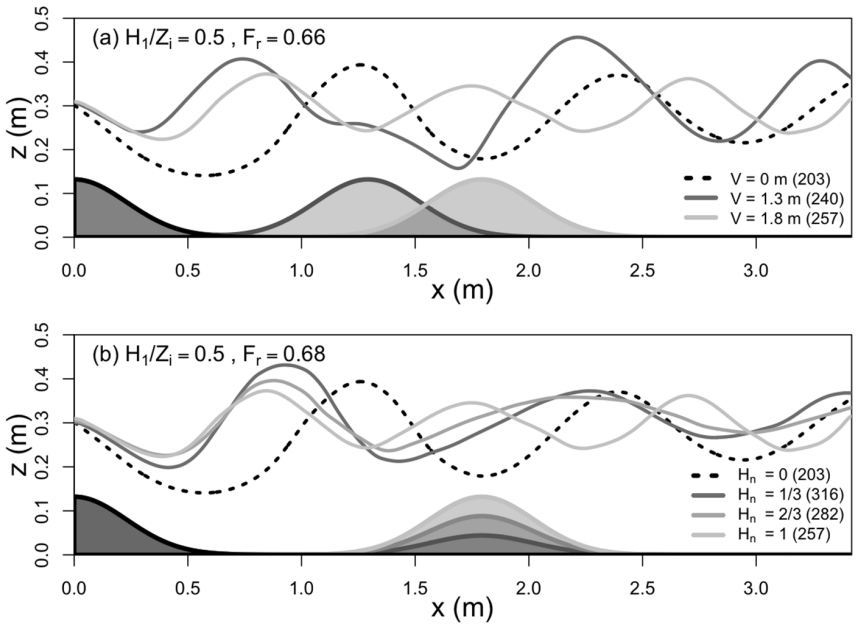

Figure 9. Same as in Figure 7, except for H_1/Z_i = 0.5 and F_r = 0.66–0.68.

To establish whether a systematic interference pattern emerges from HyIV-CNRS-SecORo experiments, amplitudes and wavelengths of double obstacle experiments are scaled by values from the corresponding experiment with a single obstacle as was done in Stiperski and Grubišić [29]. Experimental results are then compared to those from Stiperski and Grubišić [29] (their Figures 11a and 13a) The interference pattern for obstacles of equal height but different valley width is shown in Figure 10a. Different experiments are separated according to dimensionless inversion height (color) and Froude number (shape) of the points. The amplitude ratio A_2/A_s increases beyond 1 for dimensionless wavelength (V/λ_s) close to integer, and is smaller than 1 for V/λ_s close to half-integer (Figure 10a) which is a clear evidence of an interference pattern suggested by Scorer [15] and Stiperski and Grubišić [29]. The exact amount of amplitude increase or decrease (constructive or destructive interference) is not as clearly delineated as in [29], but depends on both the inversion height and Froude number, since the combination of these parameters controls flow non-linearity (cf. Equation (11) in Sachsperger et al. [41]). Still, there appears to be no systematic separation of results according to either F_r or H_1/Z_i, or their combination, that would identify one of those parameters as the dominant influence on the interference. Interestingly, amplitude-increase for constructive interference (e.g., experiment 268) and decrease for destructive interference (experiment 223) is larger than observed

by Stiperski and Grubišić [29] for both free- and no-slip simulations, in line with the hypothesis that non-linearity plays a more important role in the interference of waves trapped on the inversion than those trapped by positive wind shear. The difference to [29] could also stem from the fact that the turbulence in laboratory experiments is three-dimensional (3D) and the flow is allowed to develop in the cross-stream direction (albeit both the obstacles and the incoming flow itself are 2D), whereas the numerical simulations were fully 2D.

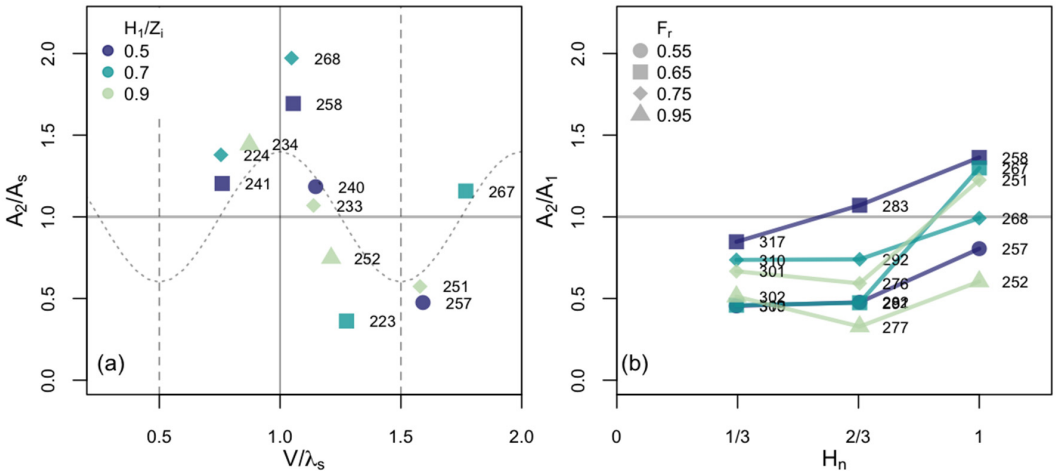

Figure 10. Interference pattern for the trapped lee-wave experiments; (**a**) Amplitude ratio A_2/A_s as a function of dimensionless valley width V/λ_s for twin obstacles (H_n = 1); (**b**) Amplitude ratio A_2/A_1 as a function of mountain height ratio H_n for experiments with equal valley width (V = 1.8 m). The color of the points corresponds to dimensionless inversion height H_1/Z_i, and the symbol to the Froude number of the experiment F_r. Vertical lines in panel (**a**) show full and half-integer values of V/λ_s indicating where constructive and destructive interference is expected. Dotted wavy line indicates possible interference pattern inspired by results of Stiperski and Grubišić [29] with the values of minima and maxima obtained from linear no-slip simulations in [29]. Colored lines in panel (**b**) connect experiments with the same set-up (F_r and H_1/Z_i).

Apart from the amplitude ratio being different from that observed by Stiperski and Grubišić [29], some of the experiments in Figure 10a have a minimum in theamplitude ratio for dimensionless wavelength that does not perfectly correspond to half-integer value. The reasons for this might lie in the non-stationarity of some of the single obstacle experiments used to normalize the double obstacle experiments (e.g., experiment 223).

The height of the second obstacle modulates the lee-wave amplitude downstream (Figure 10b), however, the exact effect is not the same for all experimental set-ups. In numerical simulations of Stiperski and Grubišić [29], a minimum in the A_2/A_1 ratio occurred for mountain height ratio approximately equal to two-thirds and was associated with maximum destructive interference, mirroring the fact that the lee-wave amplitude was reduced to approximately two-thirds of its original value at the location of the second obstacle height. Since the particular value of H_n for which maximum destructive interference occurs will be a function of both surface friction (decreasing the wave amplitude and wavelength) and V/λ, the 2:3 ratio cannot be taken as a universal value. It is therefore not surprising that only two sets of experiments (Figure 10b) show a minimum in A_2/A_1 ratio at H_n = 2:3. Three other experiments show a smaller increase of A_2/A_1 with increasing H_n. The value of the amplitude ratio A_2/A_1 = 0.2, found by Stiperski and Grubišić [29], for maximum destructive interference is observed only for experiment 277. The coarse resolution of H_n at which the experiments were performed does not allow us to examine the actual value of H_n for which destructive interference reaches a maximum for all experimental sets.

4. Discussion

Different upstream profiles employed by other laboratory studies of flow over double obstacles (linear density profile in [18,19] vs. profile with a jump used here) make a direct comparison between our and their results impossible. Still, some qualitative conclusions can be drawn. According to [18], obstacles as steep as those used in HyIV-CNRS-SecORo cause the point of flow separation from the surface to be strongly sensitive to the presence of the secondary obstacle. Gyüre and Jánosi [19] also observe a systematic shortening of the wavelength for flow over double obstacles. Both of these effects are observed (Figures 8 and 10) in our experiments despite the very different wave field: lee-wave wavelengths are shorter for double obstacles than for the corresponding single obstacle experiments and therefore the flow separates further up the slope. This wavelength reduction depends on both the second obstacle height and valley width (Figure 8) and appears to be a consequence of both flow non-linearity and interference itself. Stiperski and Grubišić [29] also noted that wavelengths can be modulated for cases of destructive interference, however, in their numerical simulations, the wavelength and amplitude of the flow within the valley was not as strongly affected by the second obstacle as observed in HyIV-CNRS-SecORo. This kind of influence on the flow within the valley is likely a result of flow non-linearity induced by the presence of an inversion [36] as well as the upstream propagation of information since $F_r < 1$ for these flows. On the other hand, the wavelength of trapped lee waves developing within the valley as a consequence of regime transition (see Section 3.2) does not show such a strong dependence on the second obstacle height, since long waves develop for supercritical flow with $F_r \approx 1$, where information propagates only downstream.

Changes in the stable stratification of the upper layer, which was not constant over our experiments, will also have an effect on trapped lee waves. Following Sachsperger et al. [37] the changes in the stable stratification above have a two-fold influence on the waves forming on the interface. The first one is reducing the lee-wave wavelength; the second is modulating which waves are able to propagate through the interface. Although this effect may account for the small discrepancies between the single obstacle regime diagram (Figure 6a) and the one from Vosper [35], it cannot explain the occurrence of trapped lee waves at very high Froude numbers for double obstacle experiments (Figure 6b–d) since NH_1/U did not vary much between the relevant single and double obstacle experiments. As shown in [37], the stratification above has additionally relatively little influence on the non-linearity of the waves on the inversion.

Another possible source of differences between our experimental results and numerical simulations might arise from differences in turbulence structure. As mentioned before, turbulence in mesoscale models, such as used by Vosper [35] and Stiperski and Grubišić [29], is parameterized whereas in the water tank it is directly generated. These numerical models [29,35] utilize one-dimensional turbulence schemes that have been shown to have limitations in representing the true interaction between mountain waves and boundary layers [42]. On the other hand, the question arises as to the how turbulent the water tank experiments are.

The Reynolds number (Re) defined based on the obstacle heights for the performed experiments ranged between 7×10^3 and 48×10^3. This value is larger than the critical value usually assumed for transition into turbulence in geophysical flows, although it is considerably smaller than in the atmosphere. Still, due to Reynolds number similarity [43], we can assume the structure of the flow to be similar once the flow is fully turbulent, irrespective of the differences in the actual magnitude of the Reynolds number. This was shown by Eiff and Bonneton [38] who examined lee-wave breaking in tanks of three different sizes (corresponding different Reynolds number ranges) in the same facility where our experiments were conducted, and showed that their results were Reynolds number independent. The fact that the transition between laminar trapped lee waves and turbulent hydraulic jumps in our experiments corresponds to that predicted by Vosper [32] gives us additional confidence that our experiments realistically reproduce geophysical turbulence.

For the correct reproduction of the lee-wave wavelength and amplitudes, however, not only the general Reynolds number of the experiments is important, but also realistic development of a turbulent

boundary layer. Unlike in [32], our experiments employed a base plate extending far upstream of the obstacle. This means that the boundary layer started to develop before reaching the obstacle. Given the length of the plate and the obstacle, and the typical towing speed, the critical Reynolds number for transition into turbulence of a flat smooth plate (5×10^5, [44]), calculated based on the distance along the plate, would still not have been reached until the lee of the first obstacle (Re ~3×10^5). However, the fact that the plate was neither smooth nor flat and that this critical Reynolds number does not account for pressure perturbations that are present in flows over obstacles, we can assume that the laminar to turbulent transition occurred already before reaching the lee of the first obstacle. The same appears to be confirmed by Knigge et al. [32] who show positive near-surface cross-stream vorticity on the lee side of the obstacle, due to friction within the boundary layer. They have not only successfully reproduced rotor flow over a range of Reynolds numbers, but the onset of rotors coincided with that predicted by Vosper [32] and also matched with the results of Large-Eddy Simulations [45]. Still, the actual value of surface roughness will have an impact on the results, because rougher surfaces cause larger reduction of wave amplitude and wavelength. Given that several experiments were conducted with a 1-m long plate covered by lego elements (having larger surface roughness), we can examine this effect. Figure 11 shows the interfaces for experiments with same H_1/Z_i and F_r but different upstream roughness. It shows that for a rougher surface, lee-wave wavelength is reduced, however, the amplitude is not significantly affected. Since no experiments were conducted with the extra rough plate and double obstacles, we are unable to say if the results would be the same given the more nonlinear interactions found for flow over double obstacles. Still, we do not expect the differences in surface roughness to alter the general conclusions of this paper in as much as lee-wave interference is expected to occur even for free-slip simulations (cf. [29]).

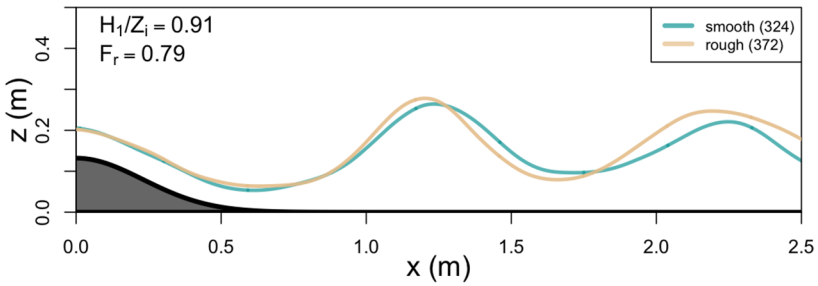

Figure 11. Interface displacement for two single obstacle runs with fixed H_1/Z_i = 0.91 and Fr = 0.79 but for a run with just the baseplate (smooth) and run with additional lego elements to increase the surface roughness (rough).

The HyIV-CNRS-SecORo experiments in the CNRM large stratified water flume have successfully reproduced the variety of flow regimes expected within the examined parameter space. One of these regimes, not addressed so far is the lee-wave rotor regime. Both Knigge et al. [32] and Vosper [35] observed rotors for H_1/Z_i larger than 0.3 and F_r larger than 0.5. This means that trapped lee wave rotors are expected over the entire trapped lee-wave regime (Figure 6) within our regime diagram. Furthermore, average obstacle steepness of 34% (calculated as the derivative of the Gaussian obstacle at the obstacle half-width) and Froude number range, places our experiments in the part of the regime diagram of Baines [46] that corresponds to post-wave separation. Whether rotors are actually observed can only be confirmed via PIV analysis and preliminary results do indeed show that our water tank experiments reproduce rotors. Still, a detailed study of rotor flow and the effect of secondary obstacles on the rotors is beyond the scope of this paper and will be a topic of a future analysis.

5. Conclusions

In the HyIV-CNRS-SecORo stratified water tank experiments, we have investigated the influence of double obstacles on the characteristics of stably stratified flow characterized by a profile with

a density jump. Lee waves trapped on the density jump and hydraulic jumps were reproduced in the water tank both for single and double obstacles. The results of single obstacle experiments were compared to previous studies in the water tank and numerical simulations and were found to agree well with both. A type of long waves, corresponding to vertically propagating waves reflected at the free water surface, were also observed in the regime where no lee waves were found in numerical simulations [35].

Consequently, the focus was placed on double obstacle experiments. The presence of a second obstacle was found to have multiple influences on the flow, depending on the flow regime. For the trapped lee wave regime, we tested the applicability of lee-wave interference theory. Both constructive and destructive interference were reproduced over twin obstacles and shown to be governed by four parameters: the dimensionless wavelength (V/λ_s), Froude number (F_r), dimensionless inversion height (H_1/Z_i) and mountain height ratio (H_2/H_1). In general, the amplitude increase for constructive interference and decrease for destructive interference was found to be larger than in the numerical simulations of Stiperski and Grubišić [29], as was the influence of the second obstacle on the flow within the valley. These differences could be due to flow non-linearity induced by the close proximity of the density jump to the obstacle top, as well as due to the fact that, unlike in the numerical simulations of Stiperski and Grubišić [29] and Vosper [35], the turbulence in HyIV-CNRS-SecORo experiments was three-dimensional. The performed experiments for different second obstacle heights did not reproduce maximum destructive interference as defined by Stiperski and Grubišić [29], except for one experiment.

Apart from lee-wave interference, HyIV-CNRS-SecORo experiments showed that the presence of the second obstacle can lead to flushing of the valley atmosphere when the lee-wave wavelength is close to or larger than the ridge separation distance. For shorter wavelengths, long waves can undergo a transition to trapped lee waves over double obstacles. Furthermore, performed experiments highlight a novel observation where long waves undergo a transition to trapped lee wave regime when the ridge separation distance is close to their wavelength over a single obstacle. In other words, trapped lee waves were observed to form in the lee of double obstacles even when the flow over a single obstacle for the same Froude numbers and dimensionless inversion height does not allow wave trapping on the density jump. A potential reason for this is the decrease of lee-wave wavelength induced by the second obstacle causing waves to become trapped on the inversion. This result suggests that a new dividing line separating the trapped lee wave regime from the long wave regime over double obstacles would be needed for our water tank experiments, but also in the atmosphere where long trapped waves, able to propagate through the inversion, can experience a shortening of their wavelength and trapping.

Supplementary Materials: The following are available online at www.mdpi.com/2073-4433/8/1/13/s1. Table S1: The full list of experiments with governing parameters: experiment number (*Nr*), Frouder number (*Fr*), dimensionless inversion height (H_1/Z_i), mountain height ratio (H_2/H_1), ridge separation distance (V), height of the first obstacle (H_1), height of the second obstacle (H_2), strength of the density jump ($\Delta\rho$), height of the density jump (Zi), Brunt-Vaisala frequency in the upper layer (N), towing speed (U), subjectively classified flow response (type: T—trapped lee waves, H—hydraulic jump, L—long waves).

Acknowledgments: We thankfully acknowledge Jean-Christophe Canonici, Frédéric Murguet and Vivian Valette for their contribution to setting up and running the experiments during the HyIV-CNRS-SecORo experiments (European Community's 7th Framework Program through the grant to the budget of the Integrating Activity HYDRALAB IV, within the Transnational Access Activities, Contract No. 261520). METEO-FRANCE contributed also to the funding of these experiments. The contribution of Radiance Calmer was supported by CNRS and Météo-France at CNRM under the supervision of Alexandre Paci and Anne Belleudy The contributions of Ivana Stiperski to this study was supported by the Austrian Science Fund (FWF) grant T781-N32. The contributions of Johannes Sachsperger, Lukas Strauss and Stefano Serafin to this study were supported by the FWF grant P24726-N27 to the University of Vienna. NCAR is funded by the National Science Foundation. We thank Charlie Dos Santos for her support to the data processing, in particular to produce composites, during her internship at CNRM supervised by Anne Belleudy and Alexandre Paci. Large parts of the contribution from Hálfdán Ágústsson were conducted during his previous affiliation with Icelandic Meteorological Office and the University of Iceland, Reykjavik, Iceland.

Author Contributions: The experiments concept is based on Ivana Stiperski PhD work supervised by Vanda Grubišić. Alexander Paci and the CNRM/GMEI/SPEA team conceived the experimental set-up and

designed the experiments in close collaboration with Ivana Stiperski, Vanda Grubišić, and Stefano Serafin.; Alexandre Paci, Radiance Calmer and Anne Belleudy performed the experiments with the help of the other coauthors; Anne Belleudy, Radiance Calmer and Alexandre Paci processed the raw data and created composites; Original concept for interface detection and processing of composites was done by Stefano Serafin and Johannes Sachsperger. Ivana Stiperski did the manual detection of interfaces and analyzed the data with contributions from Stefano Serafin.; Ivana Stiperski and Stefano Serafin interpreted the results with the contribution of Alexandre Paci; Ivana Stiperski wrote the paper and coordinated the contributions of all other coauthors.

Conflicts of Interest: The authors declare no conflict of interest. The founding sponsors had no role in the design of the study; in the collection, analyses, or interpretation of data; in the writing of the manuscript, and in the decision to publish the results.

Abbreviations

The following abbreviations are used in this manuscript:

2D	two-dimensional
3D	three-dimensional
A_s	Amplitude downstream of a single obstacle
A_1	Amplitude downstream of the first obstacle
A_2	Amplitude downstream of the second obstacle
CNRM	Centre National de Recherches Météorologiques
CNRS	Centre National de Recherches Scientifique
H_1	Height of the first obstacle
H_2	Height of the second obstacle
HyIV-CNRS-SecORo	Hydralab IV–CNRS–Secondary Orography and Rotors Experiments
λ_s	Lee-wave wavelength downstream of a single obstacle
λ_1	Lee-wave wavelength downstream of the first obstacle
λ_2	Lee-wave wavelength downstream of the second obstacle
LES	Large Eddy Simulation
PIV	Particle Image Velocimetry
T-REX	Terrain-Induced Rotor Experiment
V	ridge separation distance
Z_i	height of the density jump (i.e., inversion)

References

1. Reuder, J.; Ablinger, M.; Ágústsson, H.; Brisset, P.; Brynjólfsson, S.; Garhammer, M.; Jóhannesson, T.; Jonassen, M.O.; Kühnel, R.; Lämmlein, S.; et al. FLOHOF 2007: An overview of the mesoscale meteorological field campaign at Hofsjökull, Central Iceland. *Meteorol. Atmos. Phys.* **2011**, *116*, 1–13. [CrossRef]
2. Grubišić, V.; Sachsperger, J.; Caldeira, R.M.A. Atmospheric wake of Madeira: First aerial observations and numerical simulations. *J. Atmos. Sci.* **2015**, *72*, 4755–4776. [CrossRef]
3. Grubišić, V.; Serafin, S.; Strauss, L.; Haimov, S.J.; French, J.R.; Oolman, L.D. Wave-induced boundary layer separation in the lee of the Medicine Bow Mountains. Part II: Numerical modeling. *J. Atmos. Sci.* **2015**, *72*, 4865–4884. [CrossRef]
4. French, J.R.; Haimov, S.J.; Oolman, L.D.; Grubišić, V.; Serafin, S.; Strauss, L. Wave-induced boundary layer separation in the lee of the Medicine Bow Mountains. Part I: Observations. *J. Atmos. Sci.* **2015**, *72*, 4845–4863. [CrossRef]
5. Scorer, R.S. Theory of waves in the lee of mountains. *Q. J. R. Meteorol. Soc.* **1949**, *75*, 41–56. [CrossRef]
6. Long, R.R. Some aspects of the flow of stratified fluids: I. A theoretical investigation. *Tellus* **1953**, *5*, 42–58. [CrossRef]
7. Durran, D.R. Mountain waves. In *Mesoscale Meteorology and Forecasting*; American Meteorological Society: Boston, MA, USA, 1986; pp. 472–492.
8. Grubišić, V.; Smith, R.B.; Schär, C. The Effect of bottom friction on shallow-water flow past an isolated obstacle. *J. Atmos. Sci.* **1995**, *52*, 1985–2005. [CrossRef]
9. Smith, R.B.; Jiang, Q.; Doyle, J.D. A theory of gravity wave absorption by a boundary layer. *J. Atmos. Sci.* **2006**, *63*, 774–781. [CrossRef]
10. Jiang, Q.; Doyle, J.D.; Wang, S.; Smith, R.B. On Boundary layer separation in the lee of mesoscale topography. *J. Atmos. Sci.* **2007**, *64*, 401–420. [CrossRef]
11. Smith, C.M.; Skyllingstad, E.D. Investigation of upstream boundary layer influence on mountain wave breaking and lee wave rotors using a large-eddy simulation. *J. Atmos. Sci.* **2009**, *66*, 3147–3164. [CrossRef]

12. Guarino, M.-V.; Teixeira, M.A.C.; Ambaum, M.H.P. Turbulence generation by mountain wave breaking in flows with directional wind shear. *Q. J. R. Meteorol. Soc.* **2016**. [CrossRef]
13. Bérenger, M.; Gerbier, N. Experimental studies of lee waves in the French Alps. *Q.J.R. Meteorol. Soc.* **1961**, *87*, 13–23. [CrossRef]
14. Queney, P.; Corby, G.; Gerbier, N.; Koschmieder, H.; Zierp, J. *The Airflow Over Mountains*; WMO Technical Note; WMO: Geneva, Switzerland, 1960.
15. Scorer, R.S. *Dynamics of Meteorology and Climate*; Wiley: Chichester, UK, 1997.
16. Tampieri, F.; Hunt, J.C.R. Two-dimensional stratified fluid flow over valleys: Linear theory and a laboratory investigation. *Bound. Layer Meteorol.* **1984**, *32*, 257–279. [CrossRef]
17. Kimura, F.; Manins, P. Blocking in periodic valleys. *Bound. Layer Meteorol.* **1988**, *44*, 137–169. [CrossRef]
18. Lee, J.T.; Lawson, R.E.; Marsh, G.L. Flow visualization experiments on stably stratified flow over ridges and valleys. *Meteorol. Atmos. Phys.* **1987**, *37*, 183–194. [CrossRef]
19. Gyüre, B.; Jánosi, I.M. Stratified flow over asymmetric and double bell-shaped obstacles. *Dyn. Atmos. Oceans* **2003**, *37*, 155–170. [CrossRef]
20. Grisogono, B.; Pryor, S.C.; Keislar, R.E. Mountain wave drag over double bell-shaped orography. *Q. J. R. Meteorol. Soc.* **1993**, *119*, 199–206. [CrossRef]
21. Vosper, S. Gravity-wave drag on two mountains. *Q. J. R. Meteorol. Soc.* **1996**, *122*, 993–999. [CrossRef]
22. Mayr, G.J.; Gohm, A. 2D Airflow over a double bell-shaped mountain. *Meteorol. Atmos. Phys.* **2000**, *72*, 13–27. [CrossRef]
23. Grubišić, V.; Doyle, J.D.; Kuettner, J.; Dirks, R.; Cohn, S.A.; Pan, L.L.; Mobbs, S.; Smith, R.B.; Whiteman, C.D.; Czyzyk, S.; et al. The terrain-induced rotor experiment. *Bull. Am. Meteorol. Soc.* **2008**, *89*, 1513–1533. [CrossRef]
24. Grubišić, V.; Billings, B.J. The intense lee-wave rotor event of sierra rotors IOP 8. *J. Atmos. Sci.* **2007**, *64*, 4178–4201. [CrossRef]
25. Cohn, S.A.; Grubišić, V.; Brown, W.O.J. Wind profiler observations of mountain waves and rotors during T-REX. *J. Appl. Meteorol. Climatol.* **2010**, *50*, 826–843. [CrossRef]
26. Sheridan, P.; Vosper, S. High-resolution simulations of lee waves and downslope winds over the Sierra Nevada during T-REX IOP 6. *J. Appl. Meteorol. Climatol.* **2012**, *51*, 1333–1352. [CrossRef]
27. Strauss, L.; Serafin, S.; Grubišić, V. Atmospheric rotors and severe turbulence in a long deep valley. *J. Atmos. Sci.* **2015**, *73*, 1481–1506. [CrossRef]
28. Grubišić, V.; Stiperski, I. Lee-wave resonances over double bell-shaped obstacles. *J. Atmos. Sci.* **2009**, *66*, 1205–1228. [CrossRef]
29. Stiperski, I.; Grubišić, V. Trapped lee wave interference in the presence of surface friction. *J. Atmos. Sci.* **2011**, *68*, 918–936. [CrossRef]
30. Doyle, J.D.; Durran, D.R. The Dynamics of Mountain-Wave-Induced Rotors. *J. Atmos. Sci.* **2002**, *59*, 186–201. [CrossRef]
31. Hertenstein, R.F.; Kuettner, J.P. Rotor types associated with steep lee topography: Influence of the wind profile. *Tellus A* **2005**, *57*, 117–135. [CrossRef]
32. Knigge, C.; Etling, D.; Paci, A.; Eiff, O. Laboratory experiments on mountain-induced rotors. *Q. J. R. Meteorol. Soc.* **2010**, *136*, 442–450. [CrossRef]
33. Ágústsson, H.; Ólafsson, H. Simulations of observed lee waves and rotor turbulence. *Mon. Weather Rev.* **2014**, *142*, 832–849. [CrossRef]
34. Stiperski, I.; Ivančan-Picek, B.; Grubišić, V.; Bajić, A. Complex bora flow in the lee of Southern Velebit. *Q. J. R. Meteorol. Soc.* **2012**, *138*, 1490–1506. [CrossRef]
35. Vosper, S.B. Inversion effects on mountain lee waves. *Q. J. R. Meteorol. Soc.* **2004**, *130*, 1723–1748. [CrossRef]
36. Teixeira, M.A.C.; Argaín, J.L.; Miranda, P.M.A. Orographic drag associated with lee waves trapped at an inversion. *J. Atmos. Sci.* **2013**, *70*, 2930–2947. [CrossRef]
37. Sachsperger, J.; Serafin, S.; Grubišić, V. Lee waves on the boundary-layer inversion and their dependence on free-atmospheric stability. *Front. Earth Sci.* **2015**, *70*. [CrossRef]
38. Eiff, O.S.; Bonneton, P. Lee-wave breaking over obstacles in stratified flow. *Phys. Fluids* **2000**, *12*, 1073–1086. [CrossRef]
39. Lacaze, L.; Paci, A.; Cid, E.; Cazin, S.; Eiff, O.; Esler, J.G.; Johnson, E.R. Wave patterns generated by an axisymmetric obstacle in a two-layer flow. *Exp. Fluids* **2013**, *54*, 1618. [CrossRef]

40. Dossmann, Y.; Paci, A.; Auclair, F.; Lepilliez, M.; Cid, E. Topographically induced internal solitary waves in a pycnocline: Ultrasonic probes and stereo-correlation measurements. *Phys. Fluids* **2014**, *26*, 056601. [CrossRef]
41. Sachsperger, J.; Serafin, S.; Grubišić, V.; Stiperski, I.; Paci, A. The amplitude of lee waves on the boundary-layer inversion. *Q. J. R. Meteorol. Soc.* **2016**. [CrossRef]
42. Muñoz-Esparza, D.; Sauer, J.A.; Linn, R.R.; Kosović, B. Limitations of one-dimensional mesoscale PBL parameterizations in reproducing mountain-wave flows. *J. Atmos. Sci.* **2015**, *73*, 2603–2614. [CrossRef]
43. Wyngaard, J.C. *Turbulence in the Atmosphere*; Cambridge University Press: Cambridge, UK, 2010.
44. Oertel, H. *Prandtl's Essentials of Fluid Mechanics*; Springer: New York, NY, USA, 2004.
45. Knigge, C. Untersuchungen von Atmosphärichen Gebirgsrotoren mit Hilfe von Laborexperimenten und Grobstruktursimulationen. Ph.D. Thesis, Leibniz Universität Hannover, Hanover, Germany, 25 January 2012.
46. Baines, P.G. *Topographic Effects in Stratified Flows*; Cambridge University Press: Cambridge, UK, 1995.